Battery Energy

RESEARCH ARTICLE OPEN ACCESS

Pressure-Driven Structural Distortion in Cold Sintered $LiFePO_4|Li_{1.3}Al_{0.3}Ti_{1.7}(PO_4)_3$ Composite Solid Electrolyte Bilayers

Sergio Ferrer-Nicomedes[1,2] | Maider Zarrabeitia[3,4] | Andrés Mormeneo-Segarra[1,2] | Dominic Bresser[3,4,5] | Germà Garcia-Belmonte[6] | Nuria Vicente-Agut[1,2] | Antonio Barba-Juan[1,2]

[1]Chemical Engineering Department, Universitat Jaume I, Castelló de la Plana, Spain | [2]Instituto Universitario de Tecnología Cerámica, Universitat Jaume I, Castelló de la Plana, Spain | [3]Helmholtz Institute Ulm (HIU), Ulm, Germany | [4]Karlsruhe Institute of Technology (KIT), Karlsruhe, Germany | [5]Ulm University (UUlm), Ulm, Germany | [6]Institute of Advanced Materials, Universitat Jaume I, Castelló, Spain

Correspondence: Nuria Vicente-Agut (vicenten@uji.es)

Received: 24 September 2025 | **Revised:** 30 January 2026 | **Accepted:** 19 February 2026

Funding: Conselleria d'Educació, Investigació, Cultura i Esport, Grant/Award Numbers: MFA/2022/030, ACIF/2021/294, CIACIF/2021/050, BEFPI/2024/29; Ministerio de Ciencia e Innovación, Grant/Award Number: MCIN/AEI/10.13039/501100011033; Universitat Jaume I, Grant/Award Number: UJI/2023/016

Keywords: bilayers | cold sintering process | composite solid electrolytes | high-pressure cathode | *operando* XRD

ABSTRACT

The pressure applied during the fabrication of $LiFePO_4$-composite solid electrolyte bilayers via Cold Sintering Process (CSP) is known to influence their electrochemical performance and structural integrity. In a previous work, the authors have reported that bilayers sintered at high pressure (720 MPa) achieve high densification, but exhibit rapid capacity fading and poorer cycling stability compared to those processed at lower pressures (300 MPa). This study employs the galvanostatic intermittent titration technique (GITT), *operando* X-ray diffraction (XRD), and ex situ X-ray photoelectron spectroscopy (XPS) to elucidate the underlying mechanisms hindering the performance in high-pressure bilayers. GITT reveals larger and progressively increasing overpotentials and internal resistances, as well as irregular ion diffusion in high-pressure bilayers, suggesting altered lithiation kinetics. *Operando* XRD identifies irreversible phase transformations alongside accumulation of inactive $FePO_4$ species, with XPS confirming the presence of oxidized iron (Fe^{3+}) in the discharged cathodes sintered at high pressure. Notably, lattice distortions in the *b* and *c* axes—key lithium diffusion pathways in the olivine structure—are more pronounced at 720 MPa, indicating pressure-induced crystalline deformation modifies the energy barrier for lithium ion migration. Conversely, bilayers sintered at 300 MPa maintain stable structural and kinetic behavior, enabling reversible cycling and superior performance. These findings underscore the delicate balance required in CSP pressure to optimize densification of multi-component structures without compromising electrode functionality, guiding the design of robust solid-state bilayers and multilayers for next-generation battery technologies.

1 | Introduction

The growing demand for greener and higher-performance energy storage systems has accelerated the development of all-solid-state batteries (ASSBs) as alternatives to conventional lithium-ion batteries containing liquid electrolytes, aiming for higher energy densities and safer operating conditions [1–3]. The concept of ASSBs involves the substitution of the organic liquid electrolyte by a chemically inert solid electrolyte - including polymer membranes, inorganic ceramics, or hybrid composites—that eliminates safety hazards associated with flammable organic solvents. Additionally, it is sought to achieve

https://doi.org/10.1002/bte2.70100

an enhanced thermal stability, potentially higher energy density, and improved mechanical strength, which also opens up the possibility of using metals such as Li and Na or Si as electrodes to benefit from their theoretical high specific capacity (3860, 1166 and 3579 mAh g^{-1}, respectively) [4]. Polymer electrolytes offer mechanical flexibility, low interfacial resistance, and require simple manufacturing processes, whereas ceramic electrolytes typically exhibit superior ionic conductivity, thermal and chemical stability and mechanical strength, but require energy-intensive production routes [5–7]. With proper study and optimization, composite solid electrolytes, which integrate both polymeric and inorganic phases, can be designed to combine the properties of each component while mitigating their individual limitations [8]. Depending on the dominant phase and microstructure, composite solid electrolytes are generally classified either as Ceramic-in-Polymer (CIP) or Polymer-in-Ceramic (PIC) systems, each offering distinct advantages for tailoring the electrochemical properties to specific cell requirements [9, 10]. While CIP composites have been extensively explored, PIC architectures remain comparatively less studied, despite their potential to deliver high ionic conductivity, robust mechanical strength, and to suppress dendritic effects [11, 12].

One of the main reasons for the slow development of PICs is the ongoing challenge of fabricating dense, defect-free solid electrolytes and establishing low-resistance electrode-electrolyte interfaces. High-temperature solid-state sintering processes (>900°C) often cause the formation of secondary phases in inorganic materials, which can be detrimental to the performance, and always the decomposition of the polymer phase due to the high temperatures, limiting PIC electrolytes' implementation. Consequently, CSP has emerged as a transformative low-temperature (<300°C) densification technique that employs mid-to-high pressures and a transient liquid phase to consolidate metals, ceramics and polymeric composite materials due to the low temperature required [13–15]. Pioneering work by Randall and coworkers demonstrated the efficacy of CSP in producing dense solid electrolytes and functional composite architectures with good ionic conductivity and mechanical properties, under the working frame of the pressure solution creep theory [16, 17]. By enabling the co-processing of multilayered battery components while preserving their intrinsic electrochemical properties and reducing energy consumption, CSP offers a promising approach toward scalable manufacturing of next-generation ASSBs [18, 19].

In a previous study, we demonstrated that bilayered structures consisting of a composite solid electrolyte (CSE, 90 wt.% $Li_{1.3}Al_{0.3}Ti_{1.7}(PO_4)_3$ and 10 wt.% polyethylene oxide—lithium bis(trifluoromethanesulfonyl)imide (PEO_2–LiTFSI) composition) and a $LiFePO_4$ (LFP) cathode processed via CSP, show a strong dependence of the electrochemical performance on the sintering pressure [19]. Bilayers sintered at 720 MPa exhibited rapid capacity fading and poorer cycling stability compared with those sintered at 300 MPa, which maintained a constant specific capacity above 90 mAh $g^{-1}{}_{LFP}$ at 1C for multiple cycles. *Operando* EIS highlighted differences in cell kinetic limitations associated with sintering pressure. This suggested irreversible changes that affect the cathode structure, although the exact nature of the observed phenomena remained to be clarified.

To achieve the cold sintering of entire ASSBs with optimal properties, it is essential to understand the phenomena affecting each component of the battery under the processing conditions. While LATP-based CSEs have been extensively studied, the sensitivity of the cathode to processing variables, especially pressure, remains unknown. This work focuses on investigating the structural and chemical evolution of the LFP cathode under different sintering pressures in bilayer assemblies with LATP-based CSE, aiming to shed light on the origins of capacity degradation and support the design of improved manufacturing protocols.

2 | Experimental Section

2.1 | Materials Preparation

The $Li_{1.3}Al_{0.3}Ti_{1.7}(PO_4)_3$-based CSE bilayers, with commercial $LiFePO_4$ (Gelon Lib Group Co.) cathode active material, remain the same as those employed in the groups' previous work reporting its preparation through a CSP and the EIS characterization of the two-component structures [19] Briefly, the high sintering pressure (720 MPa) and the low sintering pressure (300 MPa) bilayers presented an ionic conductivity of 0.17 and 0.5 mS cm^{-1}, respectively. A thickness of 800 μm and surface area of 46.5 mm^2, with a cathode mass loading of 3 mg cm^{-2} (electrode thickness of 10 and 16 μm in 300 and 720 MPa, respectively). More details about the solid-state synthesis and processing and characterization of the NASICON ceramics, and the CSP setup and conditions are deeply described in the Supplementary Information and in previous works [20, 21].

2.2 | Cells Assembly

In this work, two-electrode 3/8″ Swagelok-type PFA cells are employed for the galvanostatic cycling and are assembled inside an Ar-filled glovebox (O_2 and H_2O levels below 0.1 ppm). Li metal (0.25 mm, MSE PRO) is used as the counter and reference electrode, and a glass microfiber (Whatman GF/A, 0.26 mm thick) is used as a separator to avoid the Ti^{4+}/Ti^{3+} reaction between the LATP and Li metal due to direct contact. To ensure Li^+ diffusion from the Li metal to the ceramics, 5 μL of 1 M $LiPF_6$ in EC:DMC (1:1vol., Sigma Aldrich) is employed, as the main goal of this work is to study the phenomena on the cathode side of the cell. Nonetheless, the small 2.5% open porosity of the CSEs (previously reported) and the low amount of liquid electrolyte employed allow the ceramic to act as the main electrolyte. 300 and 720 MPa bilayers employed for the surface characterization after cycling were previously discharged to the $LiFePO_4$ state and disassembled inside the glovebox without any rinsing procedure, and then transferred to the X-ray photoelectron spectroscopy (XPS) in an air-tight transfer box. For the *operando* XRD upon galvanostatic cycling, a self-designed *operando* cell developed by Bresser et al. was employed, and the half-cells were assembled as standard cells inside the glovebox [22]. The cell is made of stainless steel covered internally with a Mylar foil for electrical insulation and presents an aluminum window with a central hole where the cathode side is placed, through which the XRD is performed, acting as an electrical contact with the aluminum current collector of the cathode.

2.3 | Electrochemical and Microstructural Characterization

For the estimation of the kinetic parameters, such as the lithium-ion diffusion coefficient (D_{Li^+}, cm^2 s^{-1}), the ohmic drop, and for the comparison between series of bilayers, GITT is employed. With this technique, the voltage response of the material during a complete charge and discharge is studied by applying short galvanostatic pulses of 300 s (CC), followed by open-circuit relaxation periods of 1800 s (see Figure S1). With Equation (1), it is possible to calculate the diffusion coefficient of the cathode upon the cycling, being τ the CC pulse time (300 s), m the cathode active material mass (g), V_m the molar volume of the cathode (cm^3 mol^{-1}), MW the molecular weight (g mol^{-1}), S the electrode surface area (cm^2), ΔE_t and ΔE_s the potential change in the constant current step and in the steady state (V vs. Li$^+$/Li), respectively, and L the electrode thickness (cm).

$$D_{Li^+} = \frac{4}{\pi \cdot \tau} \cdot \left(\frac{m \cdot V_m}{MW \cdot S}\right)^2 \cdot \left(\frac{\Delta E_s}{\Delta E_t}\right)^2; \quad \tau \ll \frac{L^2}{D_{Li^+}}. \tag{1}$$

To carry on the GITT analysis, a Biologic BCS 905 battery cycler is employed, whereas for galvanostatic cycling prior to XPS surface analysis, a Maccor 4000 battery tester is used. All electrochemical measurements are done inside a climatic chamber to control the temperature at 20 ± 1°C. The potential range selected for the cycling of the cells is 2.7–4.2 V versus Li$^+$/Li, and a theoretical specific capacity of 170 mAh g$^{-1}{}_{\text{LFP}}$ for the LiFePO$_4$ is considered (1 C = 170 mA g^{-1}). The XPS is conducted with a monochromatic Al Kα ($h\nu = 1487$ eV) X-ray source, a Phoibos 150 XPS spectrometer and a microchannel plate and Delay Line Detector. The high-resolution scans are acquired using an X-ray source with a power of 200 W (12 kV), a pass energy of 30 eV, and energy steps of 0.1 eV in fixed analyzer transmission mode. The deconvolution of the spectra is performed using the CasaXPS software, with a nonlinear Shirley-type background and 70% Gaussian and 30% Lorentzian profile functions [23]. All the samples are calibrated with respect to adventitious carbons at 285 eV [24]. A focused 5 keV Ar sputtering ion beam (20 min, sputtering rate of 0.8 nm min^{-1}) is used to gain depth resolution of the cathode material to acquire more representative information about the oxidation states. *Operando* XRD (Bruker D8 ADVANCE diffractometer, Cu Kα radiation, 10°–80°, 2θ range) upon de-/lithiation is investigated in a 2θ range from 20° to 38° with a step size of 0.0297° and an overall time of about 2 h per scan in order to obtain enough resolution, using the above-mentioned two-electrode *operando* cell. The *operando* XRD cell is galvanostatically cycled using a single-channel potentiostat/galvanostat (SP-200, BioLogic), at a scan rate of 0.05 C between 2.7 and 4.2 V versus Li$^+$/Li. The Le Bail fittings of the crystalline structures from LiFePO$_4$ [*Pmna* (62), ICSD #53684] and FePO$_4$ [*Pnma* (62), ICSD #92199] from the *operando* analysis are performed using the JANA2006 program package [25–27]. The X-ray diffractograms of the as-prepared bilayers for the microstrain investigations are refined with the FullProf software.

3 | Results

In a previous investigation, electrode-solid electrolyte bilayer structures integrating the CSE (90 wt.% LATP and 10 wt.% PEO$_2$-LiTFSI) and the LiFePO$_4$ cathode were successfully produced via CSP at 150°C and a sintering pressure of 720 MPa. This pressure was previously reported to achieve high densification and acceptable ionic properties in the NASICON ceramics. However, these bilayers exhibited rapid capacity fading and reduced cycling stability [19]. Conversely, when the CSP pressure was reduced to 300 MPa, significant improvements in the ionic conductivity and cycling performance were observed while maintaining structural integrity and densification. The limitations in the high-pressure bilayers (720 MPa) were initially attributed to kinetic constraints in the cathode material, as a consequence of potential particle deformation and crystalline distortion in the LiFePO$_4$. *Operando* EIS revealed that during a single galvanostatic cycle, the charge transfer resistance (R_{ct}) doubled and the behavior of the resistance associated to the de-/lithiation mechanism (R_{Ass}) indicated inefficient energy storage, suggesting irreversible processes. Despite these observations, the physical origin of these limitations remains unclear.

In the present work, the GITT is first employed to investigate the lithiation processes under galvanostatic conditions, to further elucidate these pressure-driven kinetic limitations. First introduced by Weppner and Huggins in 1977, GITT determines kinetic parameters of electrode materials [28]. This method applies brief constant-current (CC) pulses to the electrochemical cell, each followed by open-circuit relaxation periods. By analyzing the potential response during and after each pulse, Equation (1) estimates ionic diffusion coefficients and charge-transfer kinetics in the cell, minimizing nonlinear effects while distinguishing resistive from diffusional contributions. Through quantitative analysis of ionic diffusion coefficients and cell potential variations (overpotential, Ohmic drops, ...), this technique provides essential insights into the intrinsic kinetic characteristics influencing the electrode material behavior.

Firstly, both 300 and 720 MPa bilayers are assembled in half-cells versus Li metal. GITT is performed over a complete charge and discharge cycle at 0.1 C, as shown in Figure 1a,c. After this, the cells are cycled at the same C-rate for 10 consecutive galvanostatic cycles. This cycle count is chosen because previous work showed it is enough to reveal differences in cycling behavior for 720 MPa bilayers (Figure 1e,f) [19]. Although capacity fading is less pronounced, likely due to the low cycling rate, differences in the specific capacity emerged (155 mAh g$^{-1}{}_{\text{LFP}}$ for 300 MPa and 140 mAh g$^{-1}{}_{\text{LFP}}$ for 720 MPa). Notably, voltage profiles during these 10 cycles revealed significant differences: the 720 MPa bilayer exhibited increasing overpotential during charge (Figure S2), consistent with prior report. This suggests an increase in the internal resistance, likely associated with charge transfer limitations. Immediately after cycling, a second GITT measurement is performed (Figure 1b,d). Despite the technique's long resting periods at quasi-open circuit voltage (QOCV), the 720 MPa bilayer's voltage profile is still far from the expected 3.45 V versus Li$^+$/Li plateau for LFP. Furthermore, the overpotential ($\eta_{\text{CC}} - \eta_{\text{QOCV}}$) analysis (insets of Figure 1) shows no differences between the first and the second GITT measurements for the 300 MPa bilayer (approximately 50 mV of overpotential in the plateau region). However, the 720 MPa bilayer shows not only a higher initial overpotential than the 300 MPa bilayer (90 mV vs. 50 mV), but also an increase to 150 mV after the 10 intermediate GITT cycles. This evolution during the GITT is plotted in Figure 2a,c, highlighting the divergence between the low and high pressure bilayers. While the 300 MPa bilayer maintains

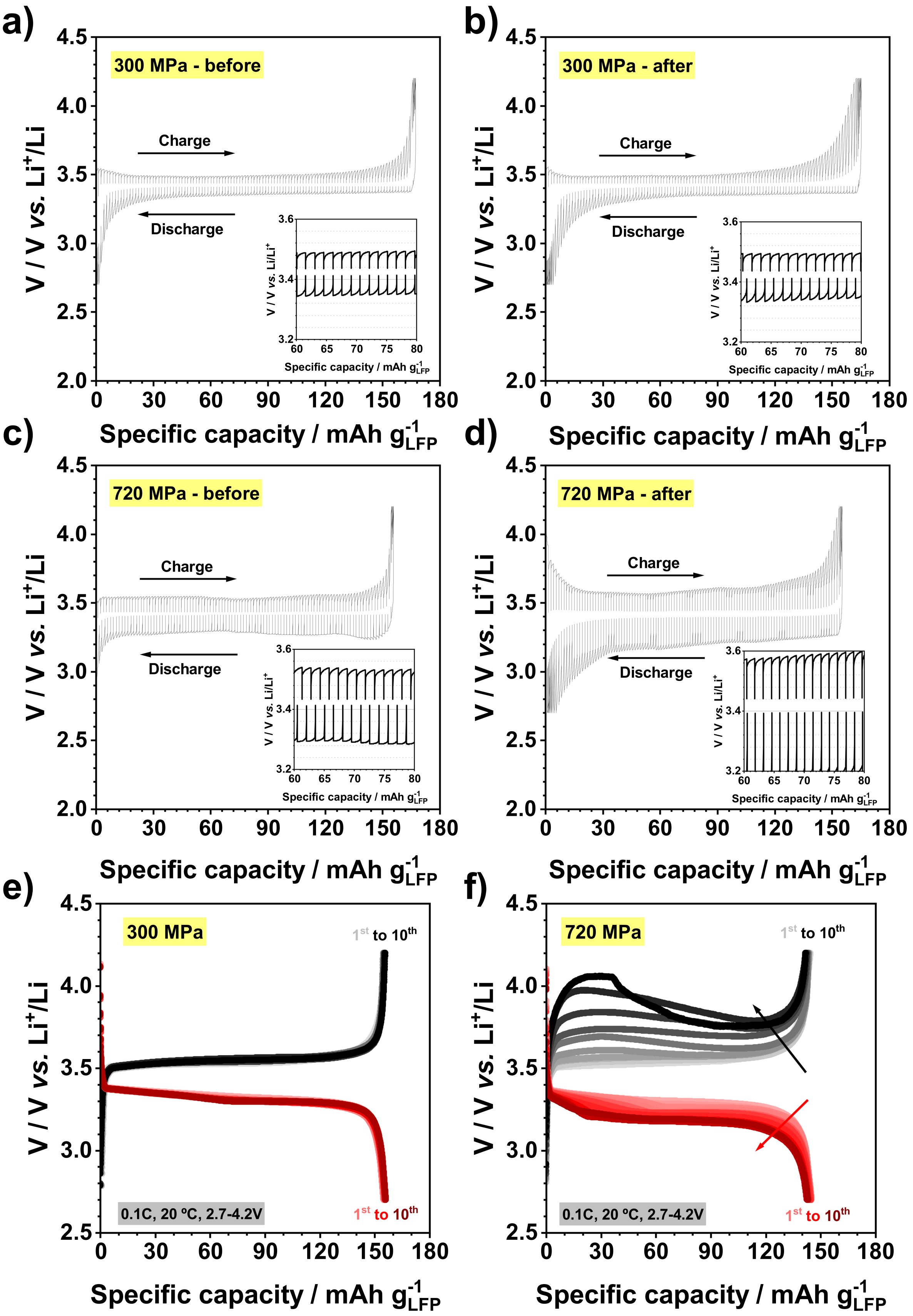

FIGURE 1 | (a, b) Voltage profile during galvanostatic intermittent titration technique (GITT) of the 300 MPa and the (c, d) 720 MPa bilayers before and after intermediate cycling. (e, f) Specific capacity profiles of the 300 and 720 MPa during the GITT intermediate cycling at 0.1 C and 20°C. Insets of the GITT plots show the detail of the overpotential at a random time during the plateau region of the cycling.

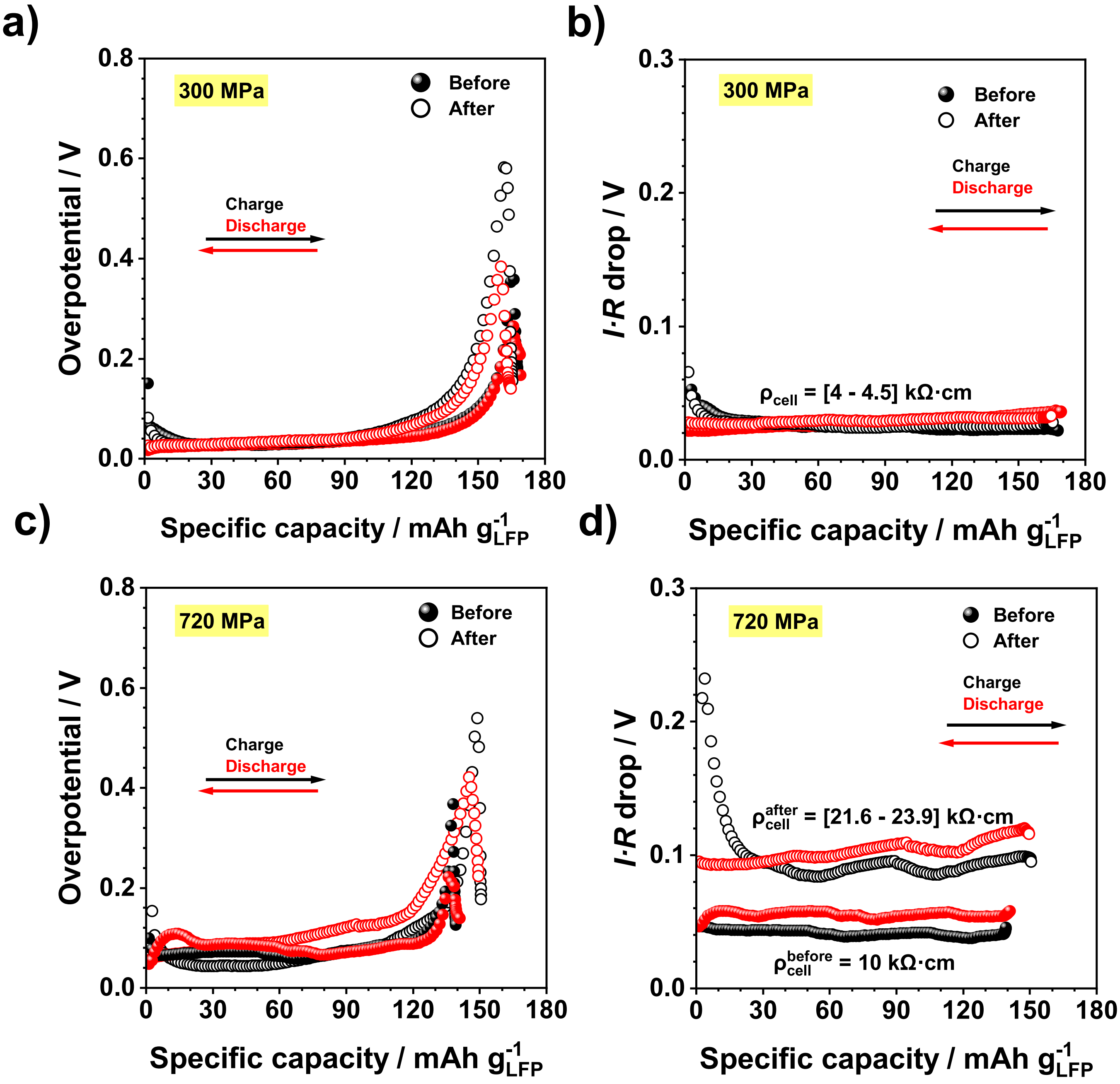

FIGURE 2 | (a, b) Overpotential and $I \cdot R$ drop versus specific capacity of the 300 MPa and (c, d) the 720 MPa bilayers extracted from the galvanostatic intermittent titration technique (GITT) analysis. Insets of these plots show the overall resistivity of the cells. In black and red colors are represented the charge and discharge procedure, and in solid and empty symbols the data from the initial and final GITT, respectively.

nearly identical overpotential profiles before and after the cycling, the 720 MPa sample displays a continuous overpotential growth within cycles during initial and post-cycling GITT measurements, indicating a progressive deterioration of the electrochemical response.

Consistent with these findings, the $I \cdot R$ drop profile (Figure 2b,d) tracks the evolution of the cell's internal resistance during cycling. $I \cdot R$ drop is intentionally presented in V, as it represents the real ohmic voltage drop experienced by the cells under operation. To enable a direct comparison between bilayers with slightly different cathode thicknesses, the resistance values extracted from the $I \cdot R$ drop are additionally expressed in the plots as an effective resistivity of the full bilayer, accounting for the electrode area and total stack thickness. This representation removes geometric effects and allows the resistive behavior of the two pressure conditions to be compared on an equivalent basis. This potential drop arises from the multiple resistive contributions: the composite solid electrolyte (R_{LATP}), the charge transfer (R_{ct}) and lithiation mechanism (R_{Ass}). In the previous work, *operando* EIS studies during galvanostatic cycling revealed that R_{LATP} remained constant, while R_{ct} and R_{Ass} dominated performance, especially in the high-pressure bilayers, in which abnormal cycling behavior indicated kinetically induced degradation at 720 MPa. In agreement with these findings, the effective resistivity derived from the $I \cdot R$ drop in the present GITT study increases twofold time resistivity during intermediate cycling in the 720 MPa bilayers (from 10 to ~22 kΩ cm), whereas it remains stable in the 300 MPa samples. Importantly, the evolution of the ohmic contribution upon cycling—rather than its absolute value—is the critical feature, as its marked increase occurs exclusively in the high-pressure bilayers and signals pressure-induced modifications in the cathode material, while the CSE remains stable.

This rise, coupled with the overpotential in high-pressure bilayers, suggests hindered electronic and Li^+ transport pathways. Furthermore, an apparent Li^+ diffusion coefficient (D_{Li^+}), as derived from the GITT analysis, is studied here in order to complement the observations of the de-/lithiation kinetics, due to the observed change in the slope of the EIS spectra in the low-frequency region in the previous report. It is worth noting that, for olivine LFP undergoing a two-phase reaction, the diffusion coefficient extracted from GITT should be interpreted as an apparent kinetic parameter rather than pure solid-state diffusivity, as it may also include phase-boundary motion or mosaic transformation effects. The analysis via GITT before and after the intermediate cycling (Figure 3) shows that for the 300 MPa bilayers the diffusion phenomenon tends to be stable during the plateau region of the LFP (consistent with previously reported values of diffusion coefficient for standard LFP cathodes, 10^{-14}–10^{-18} $cm^2 s^{-1}$) [29–31] and gradually increases as

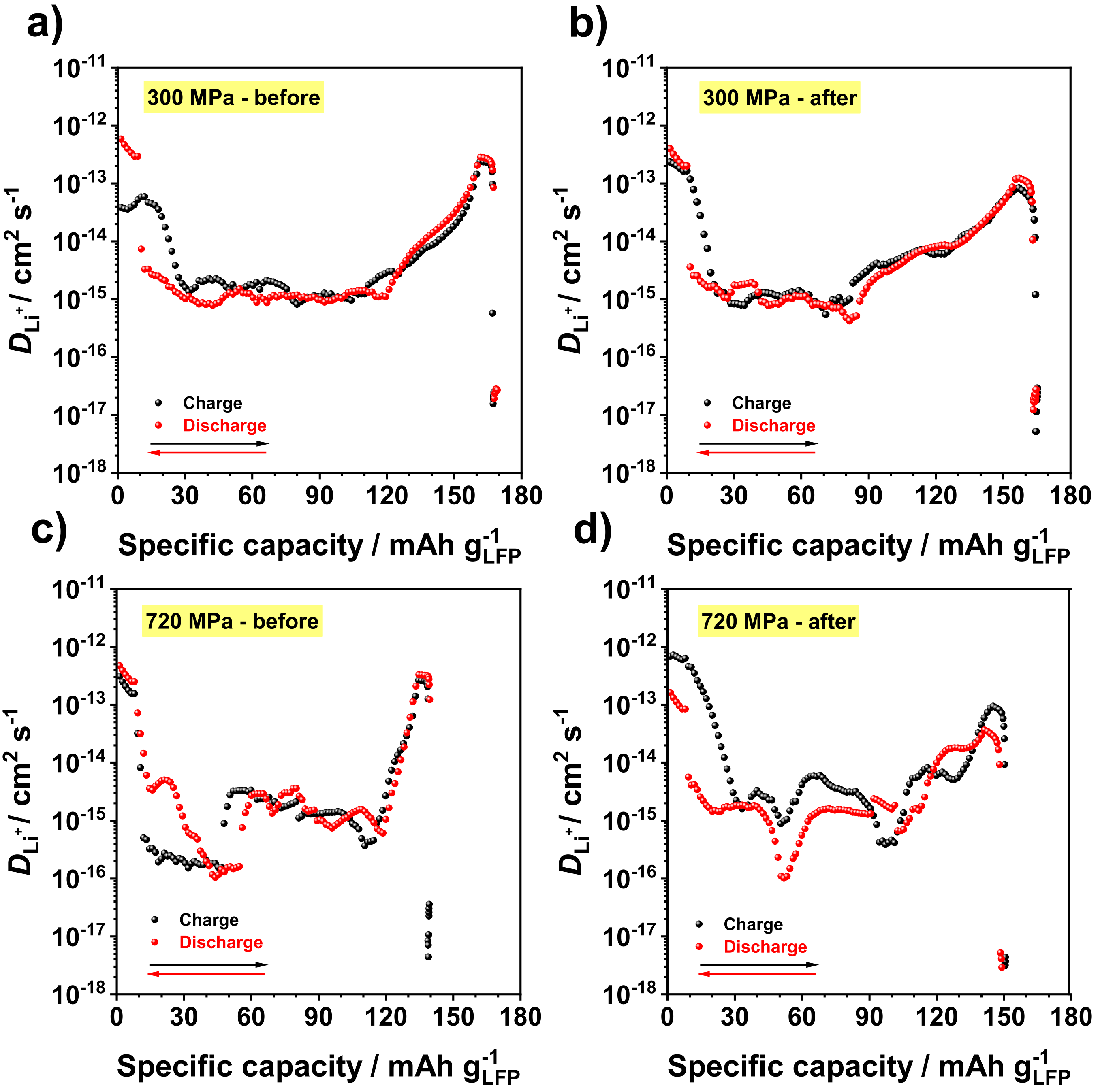

FIGURE 3 | (a, b) Apparent Li^+ diffusion coefficient versus specific capacity of the 300 MPa and (c, d) the 720 MPa bilayers calculated from the galvanostatic intermittent titration technique (GITT) analysis. In black and red colors are represented the charge and discharge procedure from the initial and final GITT, respectively.

the de-/lithiation mechanism is completed. This electrochemical behavior aligns with expected slow kinetics of the two-phase $LiFePO_4$ insertion-extraction mechanism [32]. In contrast, the profile of the apparent $D_{Li}{}^+$ of the 720 MPa bilayer is observed to be less stable, exhibiting pronounced drops during de-/lithiation, which indicates an evolving and deteriorating kinetic response rather than a well-defined two-phase transformation.

To provide more details about the oxidation state reversibility of the LFP cathode material during the cycling, ex situ XPS was performed on one fresh (before) and cycled (after) 300 and 720 MPa bilayers, with an intermediate cycling of 20 cycles at 0.1 C. Figure S3 shows the voltage profiles and specific capacity evolution of both types of bilayers, performing similarly to previous tests: the 300 MPa bilayer achieved a constant specific capacity of 160 $mAh\,g^{-1}{}_{LFP}$ with an reversible voltage profile, while the 720 MPa presented an initial specific capacity of 150 $mAh\,g^{-1}{}_{LFP}$ that faded on approximately 10 $mAh\,g^{-1}{}_{LFP}$, matching with an increasing overpotential during these 20 cycles. Regarding the XPS analysis, Figure S4 show the C 1s spectra of the cathode side for the two types of bilayers, before and after cycling, employed to calibrate all the spectra with the adventitious carbons (C–C/C–H at 285 eV) [33]. In the case of the P 2p spectra (Figure S5), all analyzed samples present the same two peaks at ~133.2 eV and ~134.1 eV corresponding to the $(PO_4)_3$—and the P 2p orbital splitting, meaning that the phosphate from the (Li)$FePO_4$ remains stable in all bilayers. Figure 4a,b displays the fitting of the Fe 2p photoelectron spectra, following the approximation of Gupta and Sen multiplet structure and the commonly employed peak splitting in iron species [34–36]. Notice that only the Fe $2p_{3/2}$ orbital is fitted for clarity. In both 300 and 720 MPa bilayers, their initial spectra indicate the presence of Fe^{2+}, corresponding to the common oxidation state of the iron in fresh LFP. After the 20 cycles at 0.1 C, the Fe 2p spectrum (Figure 4c) shows that the discharged 300 MPa bilayer remains unchanged. This confirmed a completely reversible phase transformation between $LiFePO_4$ and $FePO_4$ during the cycling. However, the 720 MPa bilayer spectrum (Figure 4d) required different conditions to those of the other Fe 2p spectra for the peaks to be fitted, due to subtle differences in the shape of the signal, involving the need of inclusion of the Fe^{3+} peaks (see Figure S6 for a comparison between the spectra with and without Fe^{3+} signal). This indicates the occurrence of irreversible processes during the LFP/FP transformation upon cycling, as the presence of Fe^{3+} traces in the spectra of the theoretically $LiFePO_4$ phase suggests that a small amount of the $FePO_4$ phase remains present in the cathode after complete discharge.

In order to unveil the phenomena responsible for the observed deterioration of the electrochemical properties in the high-pressure bilayers, *operando* XRD is performed on both types of bilayers. Samples are cycled in a half-cell configuration with the *operando* self-designed cell at a cycling rate of 0.05 C and with approximately 2 h per XRD scan to acquire sufficient X-ray signal from the cathode material during the de-/lithiation process. These, plus the well-known electrochemical stability of $LiFePO_4$ under such conditions, allow following the evolution

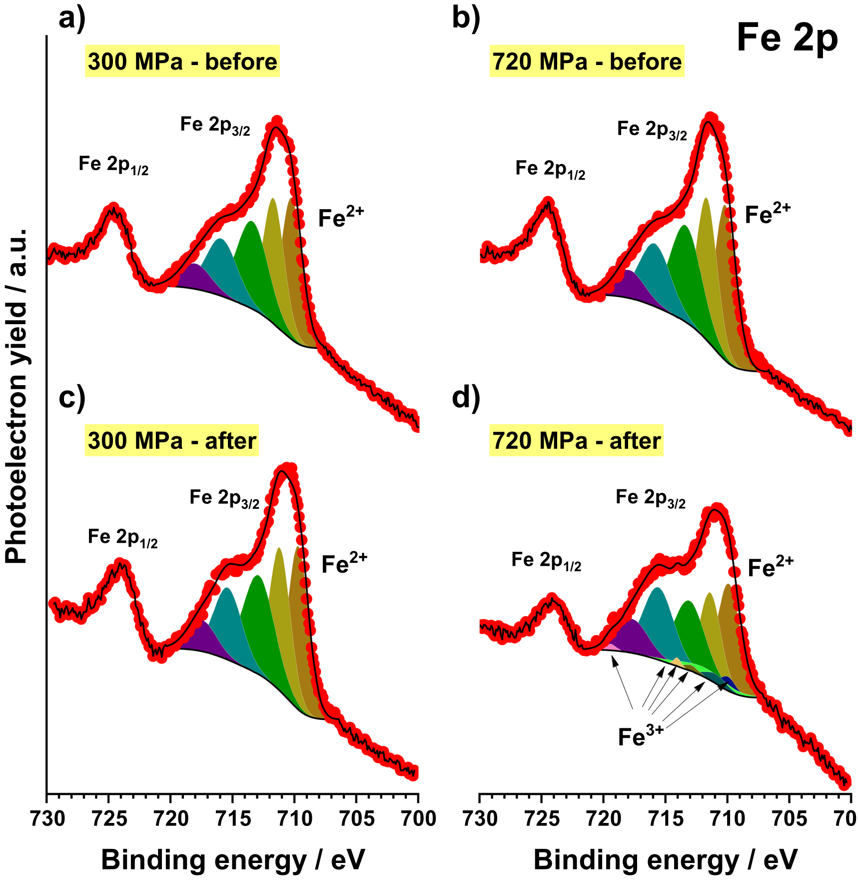

FIGURE 4 | (a, b) XPS spectra fitting of the Fe $2p_{3/2}$ species present on the fresh 300 and 720 MPa bilayers and (c, d) on the discharged 300 and 720 MPa bilayers after 20 cycles at 0.1 C and 20°C. XPS, X-ray photoelectron spectroscopy.

of the phase transformation. At this rate and during the initial cycles investigated here, the voltage plateau remains stable around 3.4 V versus Li^+/Li, as expected for a well-behaved two-phase reaction, without evidence of strong polarization or kinetic perturbations. Consequently, the number of *operando* XRD patterns per cycle can be reduced in favor of improved signal-to-noise ratio, enabling reliable discrimination between the $LiFePO_4$ and $FePO_4$ phases. This is further supported by the monotonic and progressive evolution of the diffraction patterns from one scan to the next, indicating a continuous phase transformation rather than abrupt or transient structural changes. Figure 5 summarizes all the XRD patterns during one charge and discharge for both 300 and 720 MPa, between 28° and 38° 2θ degrees. In this range, the main reflexions from $LiFePO_4$ ([020, 301, 311] and [121]) are highlighted in red, and those from $FePO_4$ ([211, 020, 311] and [121]) are highlighted in blue. One of the most evident differences between the two series is the specific capacity achieved, ~160 $mAh\,g^{-1}{}_{LFP}$ for the charge and discharge in 300 MPa, and ~130 $mAh\,g^{-1}{}_{LFP}$ for the charge of the 720 MPa, which had a capacity loss down to ~93 $mAh\,g^{-1}{}_{LFP}$ for the discharge (in the figure presented as cycling time for the sake of clarity). If the relative intensity of the peaks among the cycling is compared between the two series of samples, it can be seen that in the 720 MPa bilayers there is still a considerable amount of $LiFePO_4$ (red) present in the fully charged stated (reflections [020] and [311]), in which all the active material should be $FePO_4$. Despite this remaining unreacted phase being present in both bilayers, the intensity of these peaks in the high-pressure ones is relatively higher. This can be understood as an evidence of irreversible phase transition in the cathode—leading to less efficiency—which is in line with the lower values of initial specific capacity obtained in all cases, with respect to the theoretical 170 $mAh\,g^{-1}{}_{LFP}$ of the $LiFePO_4$. As a result, it is understood that not all the cathode active material present is available for the energy storage mechanism. Furthermore, when tracking the [020] and [311] reflections from the $FePO_4$ phase upon cycling, it is observed that these peaks appear only in the 720 MPa bilayer once the charged state is reached, but do not eventually disappear when the cell is discharged to its initial state. This is also in agreement with the XPS results, reinforcing the idea of the presence of Fe^{3+} in the discharged state. This can be directly related to the observed progressive capacity fading of the material upon cycling, which can be even intensified if the cycling rate of the cell is increased, as more inactive $FePO_4$ phase is rapidly accumulated. Liu, Q. et al. already reported this phenomenon to occur in commercial 18650 $LiFePO_4$-based lithium-ion batteries and interpreted it as loss of active lithium and capacity fading coincided with the progressive appearance of an inactive $FePO_4$ phase in the XRD data. Nonetheless, this process can be exacerbated in the cathode material of the present bilayers as the LFP electrodes are subjected to much higher sintering pressures than those subjected to classic calendering for the use in typical liquid electrolyte-based cells [37].

To further investigate the effect of pressure on the particles of the cathode active material, the lattice parameters of both types of bilayers are analyzed upon cycling and presented in Figure 6 as a function of the corresponding XRD pattern. Note that the parameters corresponding to LFP and FP are presented only when the corresponding reflections are evident in the pattern. The reference values of each lattice parameter for LFP and FP are also shown in these plots, extracted from the XRD model patterns. It can be seen at a glance that all the lattice parameters in both types of bilayers are slightly displaced from the reference values in the same way, indicating the possibility of crystalline distortion due to high CSP pressures, as suggested in previous work, though in the case of the 720 MPa bilayer, this displacement is far more evident. Further abnormal behavior is identified on both LFP and FP in the *b* and *c* lattice parameters—and thus in the cell volume—occurring in the high-pressure bilayer: once the $FePO_4$ phase appears in the cathode, the lattice parameters shrink until a certain point coinciding with the end of the charging step, and then progressively increase to the initial values. While *operando* XRD

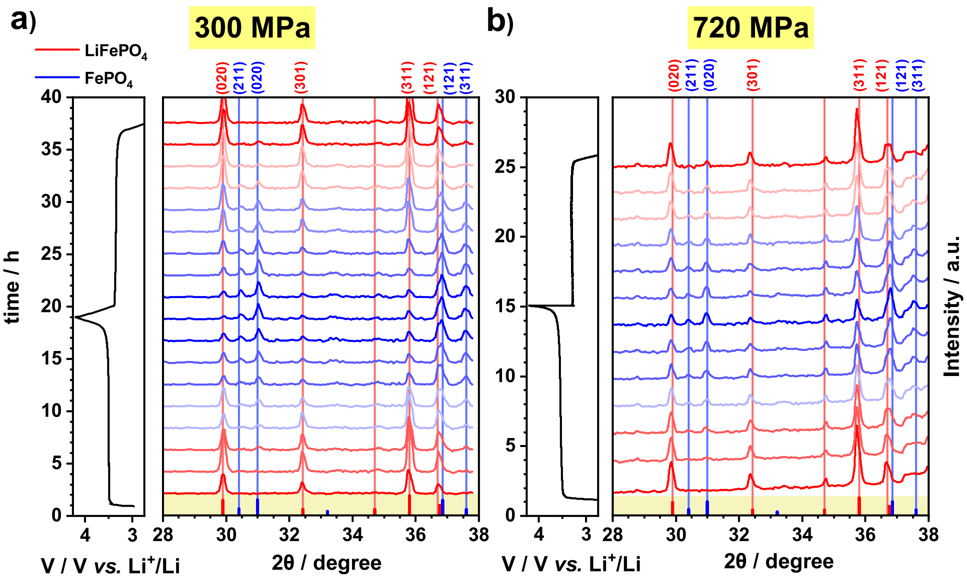

FIGURE 5 | (a) *Operando* XRD patterns of the 300 MPa and (b) 720 MPa bilayers upon cycling at 0.05 C. Main reflections and patterns of $LiFePO_4$ (red) and $FePO_4$ (blue) are displayed in red and blue, respectively. 2θ (Cu Kα) window is displayed between 28° and 38° for the sake of comparison. XRD, X-ray diffraction.

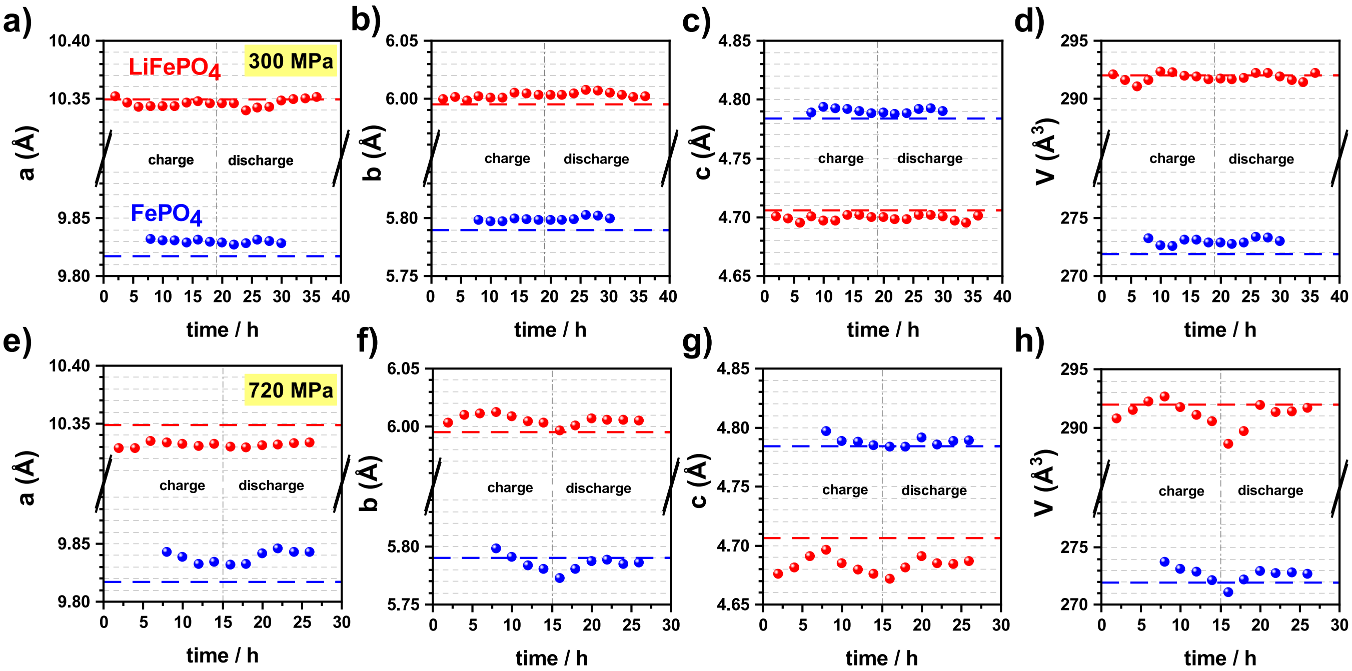

FIGURE 6 | (a, d) Lattice parameters and cell volume of the 300 MPa and (e–h) 720 MPa bilayers calculated from the *operando* XRD patterns. $LiFePO_4$ and $FePO_4$ phases are displayed in red and blue, respectively. Horizontal dashed lines highlight the value of the lattice parameter from the reference patterns ($LiFePO_4$, ICSD #53684 and $FePO_4$, ICSD #92199) [25, 26]. XRD, X-ray diffraction.

inherently probes a representative structural response within each acquisition window, the anomalous shrinkage-recovery of the b and c lattice parameters is evident in the 720 MPa bilayers and absent in the 300 MPa bilayers, indicating a pressure-induced origin. The olivine $LiFePO_4$ structure exhibits an anisotropic response due to the arrangement of its FeO_6 and PO_4 polyhedra, resulting in crystallographic directions with different mechanical compliance. Under CSP pressures approaching the GPa range, part of the applied pressure can be transferred directly into the crystallites, promoting anisotropic unit-cell compression and subtle internal distortions. This phenomenon is typically observed—with bigger lattice parameters changes—to materials presenting solid-solution phase transitions, such as the layered oxides $LiNi_{1-x-y}Mn_xCo_yO_2$ and $Li[Ni_xCo_yAl_{1-x-y}]O_2$ [38, 39]. On the contrary, olivine $LiFePO_4$ is known to undergo a two-phase transition under standard operating conditions (low to mid C-rates, no dopants and common temperatures), in which the two phases coexist during dis-/charge, independent from the model employed to describe the phase transition (core-shell, Laffont's, mosaic, domino-cascade…) [40–43]. However, it has also been reported that under severe conditions, such as high dis-/charge rates (5–10 C) or high temperatures (above 200°C), the de-/lithiation might follow a solid solution-like mechanism through metastable structures (Li_xFePO_4, $0 < x < 1$) [44, 45]. In the present case, it might be assumed that the 720 MPa bilayers undergo a solid-solution phase transformations due to the notable variation of the lattice parameters. Nonetheless, when the XRD patterns are observed in detail it is only observed the reflections corresponding to $LiFePO_4$ and $FePO_4$, without any intermediate species. Under altered two-phase transformation kinetics, transient non-equilibrium structural states may in principle occur; however, within the present experimental resolution, no additional phases or abrupt structural changes are observed.

Thus, the fluctuation of the lattice parameters and the shift with respect to the reference patterns can only be attributed to altered de/lithiation kinetics due to the high sintering pressure. These observations indicate that above a certain pressure limit, the material might start to behave as if it was under stressful operating conditions—just like very high dis-/charge rates, leading to a poor electrochemical response.

Furthermore, it is worth mentioning that the abnormal behavior of the *b*- and *c*- crystallographic axes upon cycling coincides with these being the main Li^+ diffusion pathways in the olivine structure. According to atomistic investigations, [010] is the primary migration channel for Li^+, though the [001] direction can also contribute to this diffusion, particularly at temperatures above 100°C, with a possible two-dimensional pathway [46–49]. Hence, the variation of these lattice parameters in the high-pressure bilayers is related to a deformation of the crystal, especially in the aforementioned directions. As a consequence of this modification, the main lithium diffusion pathways are affected, increasing the energy barrier for the charge transport, leading to the deteriorated electrochemical behavior in the case of the high-pressure bilayers. The effect of pressure on the Li^+ migration energy barrier was also studied by Dong, H., et. al., with a systematic in situ synchrotron XRD and DFT study, with pressures analyzed up to the GPa range [50]. The authors concluded that this energy barrier increases with the pressure along [010] and [001], although maintaining a one-dimensional ionic diffusion pathway. To examine this hypothesis in more detail, Rietveld refinement is performed on the XRD patterns of the 300 and 720 MPa bilayers immediately after CSP to gain insights into the $LiFePO_4$ microstructure of the as-prepared samples (Figure S7). The average apparent size, representing the effective coherent crystallite domain size contributing to diffraction, decreases significantly from 125.11 nm at 300 MPa to 76.89 nm at 720 MPa, reflecting pressure-induced deformation of the crystalline domains. Meanwhile, the average maximum strain shows an increase (from 16.18% to 17.98%, respectively), indicating higher microstrain levels associated with the high-pressure CSP. Hence, the constraint in the lithium transport in the cathode crystal structure can be linked to the high sintering pressure, which is eventually manifested by the increase of the internal resistance (through the $I{\cdot}R$ drop) and the increasing overpotential upon cycling in the 720 MPa bilayers, leading to poor electrochemical performance compared to the 300 MPa ones due to the irreversible behavior upon cycling. Therefore, the observed kinetic limitations due to the high-pressure CSP reported in a previous work through the *operando* EIS analysis can be attributed to the cathode's particle and crystal deformations, as confirmed in this work through a detailed microstructural characterization.

4 | Conclusion

The present study demonstrates that the pressure applied during the fabrication of $LiFePO_4$/composite solid electrolyte bilayers via Cold Sintering Process critically influences their structural properties, and in turn, its electrochemical behavior. Previous work has shown that bilayers sintered at high pressure (720 MPa) achieve high densification but also exhibit a notable electrochemical performance deterioration, including a lower specific capacity and a rapid capacity fading, compared to bilayers processed at lower pressures (300 MPa). This degradation is attributed to kinetic limitations in lithium transport within the cathode, based on previous *operando* electrochemical impedance spectroscopy results, showing increased internal resistance and hindered charge transfer at high pressure. This study provides a leap forward by using GITT and *operando* XRD to gain deeper insight into these phenomena. GITT results indicate larger and progressively increasing overpotentials and internal resistances, as well as uneven lithium diffusion coefficients in the high-pressure bilayers, signaling altered lithiation kinetics. Complementary *operando* XRD and ex situ XPS analyses reveal irreversible phase transformations characterized by accumulation of inactive $FePO_4$ species, correlating with constant capacity fading and incomplete phase reversibility. Notably, more pronounced distortions in the *b* and *c* lattice parameters—key lithium diffusion pathways in the olivine structure—are observed in the high-pressure samples, suggesting that pressure-induced crystal deformation raises the energy barrier for lithium migration. In contrast, bilayers sintered at 300 MPa maintain a stable structural and kinetic behavior, enabling more reversible cycling and superior performance. These findings underscore the delicate balance required when selecting the CSP pressure to achieve densification without compromising cathode integrity and lithium transport, ultimately affecting the reliability of the solid-state bilayers.

Author Contributions

Sergio Ferrer-Nicomedes: writing – review and editing, writing – original draft, methodology, investigation, formal analysis, data curation, conceptualization. **Maider Zarrabeitia:** writing – review and editing, investigation, formal analysis. **Andrés Mormeneo-Segarra:** writing – review and editing, investigation. **Dominic Bresser:** writing – review and editing, validation, supervision, resources. **Germà Garcia-Belmonte:** writing – review and editing, validation. **Nuria Vicente-Agut:** writing – review and editing, validation, supervision, resources, project administration, methodology, funding acquisition, formal analysis, conceptualization. **Antonio Barba-Juan:** writing – review and editing, validation, supervision, resources, project administration, methodology, funding acquisition, formal analysis, conceptualization.

Acknowledgments

This work has received funding from Generalitat Valenciana under Pla Complementari "Programa de Materials Avançats", 2022 (grant number MFA/2022/030). A. B.-J. acknowledges the financial support from Ministerio de Ciencia e Innovación (Spain) grant number. MCIN/AEI/10.13039/501100011033. N. V.-A. acknowledges the support for the research from Universitat Jaume I under the project number UJI/2023/016. A. M.-S. and S. F.-N. thank Generalitat Valenciana for the FPI Fellowship Program (grant numbers ACIF/2021/294, CIACIF/2021/050 and BEFPI/2024/29). D. B. and M. Z. would like to acknowledge financial support from the Helmholtz Association. Authors also want to acknowledge I. S.-S. and M. P. for their technical assistance and advice.

Conflicts of Interest

The authors declare no conflicts of interest.

Data Availability Statement

The data that support the findings of this study are available from the corresponding author upon reasonable request.

References

1. J. M. Tarascon and M. Armand, "Issues and Challenges Facing Rechargeable Lithium Batteries," *Nature* 414, no. 6861 (2001): 359–367, https://doi.org/10.1038/35104644.

2. J. Janek and W. G. Zeier, "A Solid Future for Battery Development," *Nature Energy* 1, no. 9 (2016): 16141, https://doi.org/10.1038/nenergy.2016.141.

3. A. Manthiram, X. Yu, and S. Wang, "Lithium Battery Chemistries Enabled by Solid-State Electrolytes," *Nature Reviews Materials* 2, no. 4 (2017): 16103, https://doi.org/10.1038/natrevmats.2016.103.

4. S. Randau, D. A. Weber, O. Kötz, et al., "Benchmarking the Performance of All-Solid-State Lithium Batteries," *Nature Energy* 5 (2020): 259–270, https://doi.org/10.1038/s41560-020-0565-1.

5. M. Armand, "Polymer Solid Electrolytes - An Overview," *Solid State Ionics* 9–10, no. PART 2 (1983): 745–754, https://doi.org/10.1016/0167-2738(83)90083-8.

6. T. Famprikis, P. Canepa, J. A. Dawson, M. S. Islam, and C. Masquelier, "Fundamentals of Inorganic Solid-State Electrolytes for Batteries," *Nature Materials* 18, no. 12 (2019): 1278–1291, https://doi.org/10.1038/S41563-019-0431-3.

7. C. Li, Z. Wang, Z. He, et al., "An Advance Review of Solid-State Battery: Challenges, Progress and Prospects," *Sustainable Materials and Technologies* 29 (2021): e00297, https://doi.org/10.1016/J.SUSMAT.2021.E00297.

8. T. Zhang, W. He, W. Zhang, et al., "Designing Composite Solid-State Electrolytes for High Performance Lithium Ion or Lithium Metal Batteries," *Chemical Science* 11, no. 33 (2020): 8686–8707, https://doi.org/10.1039/D0SC03121F.

9. L. Chen, Y. Li, S.-P. Li, L.-Z. Fan, C.-W. Nan, and J. B. Goodenough, "PEO/Garnet Composite Electrolytes for Solid-State Lithium Batteries: From "Ceramic-in-Polymer" to "Polymer-in-Ceramic."," *Nano Energy* 46 (2018): 176–184, https://doi.org/10.1016/j.nanoen.2017.12.037.

10. W. Lee, C. K. Lyon, J. H. Seo, et al., "Ceramic–Salt Composite Electrolytes From Cold Sintering," *Advanced Functional Materials* 29, no. 20 (2019): 1807872, https://doi.org/10.1002/ADFM.201807872.

11. H. Huo, Y. Chen, J. Luo, X. Yang, X. Guo, and X. Sun, "Rational Design of Hierarchical "Ceramic-in-Polymer" and "Polymer-in-Ceramic" Electrolytes for Dendrite-Free Solid-State Batteries," *Advanced Energy Materials* 9, no. 17 (2019): 1804004, https://doi.org/10.1002/aenm.201804004.

12. X. Yu and A. Manthiram, "A Review of Composite Polymer-Ceramic Electrolytes for Lithium Batteries," *Energy Storage Materials* 34 (2021): 282–300, https://doi.org/10.1016/j.ensm.2020.10.006.

13. H. Guo, A. Baker, J. Guo, and C. A. Randall, "Protocol for Ultralow-Temperature Ceramic Sintering: An Integration of Nanotechnology and the Cold Sintering Process," *ACS Nano* 10, no. 11 (2016): 10606–10614, https://doi.org/10.1021/acsnano.6b03800.

14. H. Guo, A. Baker, J. Guo, and C. A. Randall, "Cold Sintering Process: A Novel Technique for Low-Temperature Ceramic Processing of Ferroelectrics," *Journal of the American Ceramic Society* 99, no. 11 (2016): 3489–3507, https://doi.org/10.1111/JACE.14554.

15. T. Ibn-Mohammed, C. A. Randall, K. B. Mustapha, et al., "Decarbonising Ceramic Manufacturing: A Techno-Economic Analysis of Energy Efficient Sintering Technologies in the Functional Materials Sector," *Journal of the European Ceramic Society* 39, no. 16 (2019): 5213–5235, https://doi.org/10.1016/J.JEURCERAMSOC.2019.08.011.

16. A. Ndayishimiye, S. H. Bang, C. J. Spiers, and C. A. Randall, "Reassessing Cold Sintering in the Framework of Pressure Solution Theory," *Journal of the European Ceramic Society* 43, no. 1 (2023): 1–13, https://doi.org/10.1016/J.JEURCERAMSOC.2022.09.053.

17. J. Guo, X. Zhao, T. Herisson De Beauvoir, et al., "Recent Progress in Applications of the Cold Sintering Process for Ceramic–Polymer Composites," *Advanced Functional Materials* 28, no. 39 (2018): 1801724, https://doi.org/10.1002/ADFM.201801724.

18. J. H. Seo, J. Guo, H. Guo, et al., "Cold Sintering of a Li-Ion Cathode: $LiFePO_4$-Composite With High Volumetric Capacity," *Ceramics International* 43, no. 17 (2017): 15370–15374, https://doi.org/10.1016/J.CERAMINT.2017.08.077.

19. S. Ferrer-Nicomedes, A. Mormeneo-Segarra, N. Vicente-Agut, A. Barba-Juan, and G. Garcia-Belmonte, "Electrochemical Response of Cold-Sintered Cathode-Hybrid Electrolyte Bilayers: Deep Insights into the Determining Kinetic Mechanisms via Operando Electrochemical Impedance Characterization," *Energy & Environmental Materials* 8, no. 4 (2025): e12886, https://doi.org/10.1002/eem2.12886.

20. A. Mormeneo-Segarra, S. Ferrer-Nicomedes, N. Vicente-Agut, and A. Barba-Juan, "In Operando Characterization of the Ionic Conductivity Dependence on Liquid Transient Phase and Microstructure of Cold-Sintered Bi_2O_3-Doped $Li_{1.3}Al_{0.3}Ti_{1.7}(PO_4)_3$ Solid-State Electrolyte," *Ceramics International* 49, no. 22 (2023): 36497–36506, https://doi.org/10.1016/J.CERAMINT.2023.08.333.

21. S. Ferrer-Nicomedes, A. Mormeneo-Segarra, N. Vicente-Agut, and A. Barba-Juan, "Fine-Tuning the Microstructure for Improved Performance in Cold-Sintered $Li_{1.3}Al_{0.3}Ti_{1.7}(PO_4)_3$ Composite Solid Electrolytes," *Ceramics International* 50, no. 21 (2024): 44330–44338.

22. D. Bresser, E. Paillard, R. Kloepsch, et al., "Carbon Coated $ZnFe_2O_4$ Nanoparticles for Advanced Lithium-Ion Anodes," *Advanced Energy Materials* 3, no. 4 (2013): 513–523, https://doi.org/10.1002/AENM.201200735.

23. J. Walton, P. Wincott, N. Fairley, and A. Carrick, *Peak Fitting with CasaXPS: A Casa Pocket Book* (Accolyte Science, 2010).

24. C. D. Wanger, W. M. Riggs, L. E. Davis, J. F. M, and G. E. M, "Handbook of X-Ray Photoelectron Spectroscopy," *Surface and Interface Analysis* 3 (1981): v, https://doi.org/10.1002/sia.740030412.

25. M. Thiebaut, C. Billing, D. Naidoo, and D. G. Billing, "The Influence of the Li^+ Addition Rate During the Hydrothermal Synthesis of $LiFePO_4$ on the Average and Local Structure," *Dalton Transactions* 51, no. 47 (2022): 18176–18186, https://doi.org/10.1039/D2DT01752K.

26. A. Andersson, "Lithium Extraction/Insertion in $LiFePO_4$: An X-Ray Diffraction and Mössbauer Spectroscopy Study," *Solid State Ionics* 130, no. 1–2 (2000): 41–52, https://doi.org/10.1016/S0167-2738(00)00311-8.

27. V. Petrícek, M. Dušek, and L. Palatinus, "Crystallographic Computing System JANA2006: General Features," *Zeitschrift fur Kristallographie* 229, no. 5 (2014): 345–352, https://doi.org/10.1515/ZKRI-2014-1737/MACHINEREADABLECITATION/RIS.

28. W. Weppner and R. A. Huggins, "Determination of the Kinetic Parameters of Mixed-Conducting Electrodes and Application to the System Li3Sb," *Journal of the Electrochemical Society* 124, no. 10 (1977): 1569–1578, https://doi.org/10.1149/1.2133112.

29. X.-C. Tang, L.-X. Li, Q.-L. Lai, X.-W. Song, and L.-H. Jiang, "Investigation on Diffusion Behavior of Li^+ in LiFePO4 by Capacity Intermittent Titration Technique (CITT)," *Electrochimica Acta* 54, no. 8 (2009): 2329–2334, https://doi.org/10.1016/j.electacta.2008.10.065.

30. A. V. Churikov, A. V. Ivanishchev, I. A. Ivanishcheva, V. O. Sycheva, N. R. Khasanova, and E. V. Antipov, "Determination of Lithium Diffusion Coefficient in $LiFePO_4$ Electrode by Galvanostatic and Potentiostatic Intermittent Titration Techniques," *Electrochimica Acta* 55, no. 8 (2010): 2939–2950, https://doi.org/10.1016/j.electacta.2009.12.079.

31. K. Tang, X. Yu, J. Sun, H. Li, and X. Huang, "Kinetic Analysis on $LiFePO_4$ Thin Films by CV, GITT, and EIS," *Electrochimica Acta* 56, no. 13 (2011): 4869–4875, https://doi.org/10.1016/j.electacta.2011.02.119.

32. A. K. Padhi, K. S. Nanjundaswamy, and J. B. Goodenough, "Phospho-Olivines as Positive-Electrode Materials for Rechargeable Lithium Batteries," *Journal of the Electrochemical Society* 144, no. 4 (1997): 1188–1194, https://doi.org/10.1149/1.1837571/XML.

33. G. Beamson, and D. Briggs, *High Resolution XPS of Organic Polymers: The Scienta ESCA300 database* (John Wiley and Sons, 1992).

34. R. P. Gupta and S. K. Sen, "Calculation of Multiplet Structure of Core P-Vacancy Levels. II," *Physical Review B* 12, no. 1 (1975): 15–19, https://doi.org/10.1103/PhysRevB.12.15.

35. M. C. Biesinger, B. P. Payne, A. P. Grosvenor, L. W. M. Lau, A. R. Gerson, and R. S. C. Smart, "Resolving Surface Chemical States in XPS Analysis of First Row Transition Metals, Oxides and Hydroxides: Cr, Mn, Fe, Co and Ni," *Applied Surface Science* 257, no. 7 (2011): 2717–2730, https://doi.org/10.1016/J.APSUSC.2010.10.051.

36. A. E. Hughes, C. D. Easton, T. R. Gengenbach, M. C. Biesinger, and M. Laleh, "Interpretation of Complex X-Ray Photoelectron Peak Shapes. I. Case Study of Fe 2p3/2 Spectra," *Journal of Vacuum Science & Technology. A* 42, no. 5 (2024): 53205, https://doi.org/10.1116/6.0003804/3309427.

37. Q. Liu, Y. Liu, F. Yang, et al., "Capacity Fading Mechanism of the Commercial 18650 $LiFePO_4$-Based Lithium-Ion Batteries: An In Situ Time-Resolved High-Energy Synchrotron XRD Study," *ACS Applied Materials & Interfaces* 10, no. 5 (2018): 4622–4629, https://doi.org/10.1021/ACSAMI.7B13060/ASSET/IMAGES/LARGE/AM-2017-13060G_0007.JPEG.

38. S. Liu, P. J. West, H. Zhong, et al., "Origin of Phase Separation in Ni-Rich Layered Oxide Cathode Materials During Electrochemical Cycling," *Chemistry of Materials* 35, no. 21 (2023): 8857–8871, https://doi.org/10.1021/ACS.CHEMMATER.3C00924/ASSET/IMAGES/LARGE/CM3C00924_0010.JPEG.

39. H. H. Ryu, N. Y. Park, J. H. Seo, et al., "A Highly Stabilized Ni-Rich NCA Cathode for High-Energy Lithium-Ion Batteries," *Materials Today* 36 (2020): 73–82, https://doi.org/10.1016/J.MATTOD.2020.01.019.

40. A. K. Padhi, K. S. Nanjundaswamy, and J. B. Goodenough, "Phospho-Olivines as Positive-Electrode Materials for Rechargeable Lithium Batteries," *Journal of the Electrochemical Society* 144, no. 4 (1997): 1188–1194, https://doi.org/10.1149/1.1837571/XML.

41. L. Laffont, C. Delacourt, P. Gibot, et al., "Study of the $LiFePO_4$/$FePO_4$ two-Phase System by High-Resolution Electron Energy Loss Spectroscopy," *Chemistry of Materials* 18, no. 23 (2006): 5520–5529, https://doi.org/10.1021/CM0617182/ASSET/IMAGES/LARGE/CM0617182F00010.JPEG.

42. G. Brunetti, D. Robert, P. Bayle-Guillemaud, et al., "Confirmation of the Domino-Cascade Model by Lifepo4/Fepo 4 Precession Electron Diffraction," *Chemistry of Materials* 23, no. 20 (2011): 4515–4524, https://doi.org/10.1021/CM201783Z/ASSET/IMAGES/CM-2011-01783Z_M004.GIF.

43. L.-X. Yuan, Z.-H. Wang, W.-X. Zhang, et al., "Development and Challenges of $LiFePO_4$ Cathode Material for Lithium-Ion Batteries," *Energy & Environmental Science* 4, no. 2 (2011): 269–284, https://doi.org/10.1039/C0EE00029A.

44. C. Delacourt, P. Poizot, J. M. Tarascon, and C. Masquelier, "The Existence of a Temperature-Driven Solid Solution in Li $XFePO_4$ for $0 \leq x \leq 1$," *Nature Materials* 4, no. 3 (2005): 254–260, https://doi.org/10.1038/NMAT1335;KWRD=MATERIALS+SCIENCE.

45. M. Hess, T. Sasaki, C. Villevieille, and P. Novák, "Combined Operando X-Ray Diffraction–Electrochemical Impedance Spectroscopy Detecting Solid Solution Reactions of $LiFePO_4$ in Batteries," *Nature Communications* 6, no. 1 (2015): 8169, https://doi.org/10.1038/ncomms9169.

46. B. Ellis, L. K. Perry, D. H. Ryan, and L. F. Nazar, "Small Polaron Hopping in $LixFePO_4$ Solid Solutions: Coupled Lithium-Ion and Electron Mobility," *Journal of the American Chemical Society* 128, no. 35 (2006): 11416–11422, https://doi.org/10.1021/JA0614114/ASSET/IMAGES/LARGE/JA0614114H00002.JPEG.

47. C. Ouyang, S. Shi, Z. Wang, X. Huang, and L. Chen, "First-Principles Study of Li Ion Diffusion in $LiFePO_4$," *Physical Review B* 69 (2004): 104303, https://doi.org/10.1103/PhysRevB.69.104303.

48. G. K. P. Dathar, D. Sheppard, K. J. Stevenson, and G. Henkelman, "Calculations of Li-Ion Diffusion in Olivine Phosphates," *Chemistry of Materials* 23 (2011): 4032–4037, https://doi.org/10.1021/cm201604g.

49. S. E. Boulfelfel, G. Seifert, and S. Leoni, "Atomistic Investigation of Li^+ Diffusion Pathways in the Olivine $LiFePO_4$ Cathode Material," *Journal of Materials Chemistry* 21, no. 41 (2011): 16365–16372, https://doi.org/10.1039/C1JM10725A.

50. H. Dong, H. Guo, Y. He, et al., "Structural Stability and Li-Ion Transport Property of $LiFePO_4$ under High-Pressure," *Solid State Ionics* 301 (2017): 133–137, https://doi.org/10.1016/J.SSI.2017.01.026.

Supporting Information

Additional supporting information can be found online in the Supporting Information section.

Figure S1: GITT scheme of the voltage profile during the CC short pulse phase and the subsequent open-circuit relaxation period. **Figure S2:** (a) Cycling performance of the 300, 500 and 720 MPa bilayers at C/10 after the initial cycle. (b-c) The discharge (dark color) and charge (light color) capacity of 300 MPa (black) and 720 MPa (red) bilayers at C/5 and 1C, respectively. (d) Third (solid line) and last (dashed line) charge and discharge curves of the 300 and 720 MPa bilayers at C/5 and 1C. All the cycling tests are conducted in the range of 2.7–4.2 V *vs* Li^+/Li at 25°C. (Reproduced with permission from Ferrer-Nicomedes, S. et al. Energy Environ. Mater. 2025, 8, e12886). **Figure S3:** (a) Voltage profile and (b) specific capacity as a function of the cycle number before XPS analysis. Data in blue and red correspond to the 300 and 720 MPa bilayers, respectively. **Figure S4:** XPS spectra in the C 1s region of (a, c) the 300 MPa bilayer and (b, d) the 720 MPa bilayer. **Figure S5:** XPS spectra in the P 2p region of **a), c)** the 300 MPa bilayer and **b), d)** the 720 MPa bilayer. **Figure S6.** XPS spectra in the Fe 2p region for the 720 MPa bilayer, comparing the signal fitted (a) with and (b) without Fe^{3+} traces. **Figure S7:** Rietveld refinement of the bilayer XRD patterns of (a) the 300 MPa and (b) the 720 MPa samples after CSP.